Revisiting the tropical Atlantic western boundary circulation from a 25-year time series of satellite altimetry data

Djoirka Minto Dimoune[1,4], Florence Birol[2], Fabrice Hernandez[1,2], Fabien Léger[2], Moacyr Araujo[1,3]

[1]Laboratorio de Oceanografia Física Estuarina e Costeira (LOFEC), Departamento de Oceanografia da Universidade Federal de Pernambuco (UFPE), Cidade Universitária, Avenida Arquitetura s/n, 50740-550 Recife, PE, Brazil
[2]LEGOS, Université de Toulouse, CNES, CNRS, IRD, 14 avenue Edouard Belin, 31400, France
[3]Brazilian Research Network on Global Climate Change (Rede CLIMA), Av. dos Astronautas, 1758, 01227-010 São José dos Campos, SP, Brazil
[4]Nansen Tutu Center for Marine Environmental Research, Dept of Oceanography, University of Cape Town, Rondebosch, Cape Town, 7700, South Africa

Correspondance to: Djoirka M. Dimoune (pmintodimoune@gmail.com)

Abstract. Geostrophic currents derived from altimetry are used to investigate the surface circulation in the Western Tropical Atlantic over the 1993-2017 period. Using six horizontal sections defined to capture the current branches of the study area, we investigate their respective variations at both seasonal and interannual time-scales as well as the spatial distribution of these variations in order to highlight the characteristics of the currents on their route. Our results show that the central branch of the South Equatorial Current, its northern branch near the Brazilian coast, the North Brazil Current component located south of the equator and the Guyana Current have similar annual cycles, with maxima/minima during late boreal winter/boreal fall when the Intertropical Convergence Zone is at its southernmost/northern location. In contrast, the seasonal cycles of the North Brazil Current branch located between the equator and 7-8° N, its retroflected branch, the northern branch of the South Equatorial Current to the west of 35° W and the North Equatorial Countercurrent show maxima/minima during late boreal summer/boreal spring following the remote wind stress curl strength variation. West of 32° W, an eastward current is observed between 0°-2° N, identified as the equatorial extension of the retroflected branch of the North Brazil Current. It is part of a large cyclonic circulation observed between 0°-6° N and 35°-45° W during boreal spring. We also observed a secondary North Brazil Current retroflection flow during the second half of the year which leads to the two-core structure of the North Equatorial Countercurrent, and might be related to the wind stress curl seasonal changes. Eastward, the North Equatorial Countercurrent weakens and its two-core structure is underdeveloped due to the weakening of the wind stress. At interannual scales,

36 depending on which side of the equator, the North Brazil Current exhibits two opposite
37 scenarios related to the tropical Atlantic Meridional Mode phases. The interannual variability
38 of the North Equatorial Countercurrent and of the northern branch of the South Equatorial
39 Current (in terms of both strength and/or latitudinal shift) at 42° W are also associated to the
40 Atlantic Meridional Mode. However, they are associated to the Atlantic mode phases at 32° W.

41

1   Introduction

43 The energetic Western Tropical Atlantic (WTA) boundary surface circulation is known to play
44 a key role in the transport of heat, salt and water mass from the southern to the northern
45 hemispheres of the Atlantic Ocean. It corresponds to a superposition of the return branch of the
46 thermohaline Atlantic Meridional Overturning Circulation (AMOC), the flow from the
47 Subtropical Cells and Sverdrup dynamics (Schmitz and McCartney, 1993; Schott et al., 2004,
48 2005; Rodrigues et al., 2007, Tuchen et al., 2019, 2020). The region is also known to be
49 influenced by large mesoscale activities due to the barotropic instabilities of the currents. The
50 most dominant mesoscale structures are the large rings generated by North Brazilian Current
51 (NBC) retroflection (Aguedjou et al., 2019; Aroucha et al., 2020). A regional scheme of the
52 surface currents in the study area is proposed in Fig. 1. It is derived from a global analysis of
53 the different studies mentioned hereafter.

54 From 5° S to 15° N, the surface boundary circulation is formed by the NBC flowing northward
55 along the South American shelf. It carries tropical waters originating from the South Atlantic
56 subtropical gyre and contributes to interhemispheric water transport (Johns et al., 1990; 1998;
57 Peterson and Stramma, 1991; Stramma and England, 1999; Fratantoni et al., 2000; Silva et al.,
58 2009; Zheng and Giese, 2009; Garzoli and Matano, 2011). The NBC has its origin near 5° S,
59 with two sources: the central branch of the westward South Equatorial Current (cSEC); and the
60 along-shelf equatorward North Brazil Undercurrent (NBUC) which surfaces around 5-6° S
61 (Schott et al., 1998, Dossa et al., 2020). The latter advects warm waters from the South
62 Equatorial Current (SEC) through its southern branch (Schott et al., 1995; Luko et al., 2021).
63 Further north, around 5° N, the NBC is also fed by the northern branch of the SEC (nSEC)
64 (Goes et al., 2005). Then, between 5°-9° N and 45-50° W, a large part of the NBC retroflects
65 to form a southeastward retroflected branch (called hereinafter rNBC). Between 3° N and 8° N,
66 this branch first feeds the eastward North Equatorial Countercurrent (NECC) throughout the
67 year, except during the boreal spring. At that time, the NECC is fed only by the North Equatorial

2

68 Current (NEC) (Bourlès et al., 1999a; Goes et al., 2005). The NECC flows eastward between

69 2° N and 12° N, and crosses the tropical Atlantic (Didden and Schott, 1992; Ffield, 2005;

70 Urbano et al., 2008; Araujo et al., 2017). During the second half of the year, this current shows

71 two cores that can separate into a southern and a northern branch (called sNECC and nNECC,

72 respectively: Urbano et al., 2006; 2008).

73 At depth, around 3-8° N, Cochrane et al. (1979) and Schott et al. (2004) suggested that, part of

74 the rNBC also feeds the eastward North Equatorial UnderCurrent (NEUC) located around 5°

75 N. In addition, between 2° S and 3° N, the rNBC feeds the subsurface eastward Equatorial

76 UnderCurrent (EUC) (Hisard and Hénin, 1987; Bourlès et al., 1999b; Hazeleger et al., 2003;

77 Hazeleger et de Vries, 2003; Schott et al., 1995; 2004). North of 10° N, the part of the NBC

78 which has not retroflected flows northwestward along the Guyana coast, forming the Guyana

79 Current. The latter is also fed seasonally by the NEC (Johns et al., 1998) and transports warm

80 equatorial waters into the Caribbean Sea (Stramma and Schott, 1999; Garzoli et al., 2003).

81 The WTA boundary surface circulation is wind-driven. In the vorticity equation, the terms that

82 dominate localy are the Ekman pumping and the divergence of the geostrophic currents (Garzoli

83 and Katz, 1983; Urbano et al., 2006). North of the equator, the region is characterized by strong

84 seasonal variability of the wind. The Trade Winds variations influence the current system

85 formed by the NBC, the NBC retroflection (NBCR), the rNBC and the NECC. In particular the

86 NBCR location, the NBC transport and the NECC position/transport respond to the seasonal

87 changes in the wind regimes (Johns et al., 1990; 1998; Garzoli et al., 2003; 2004; Urbano et al.,

88 2006; 2008). This wind influence, which is related to the seasonal migration of the Intertropical

89 Convergence Zone (ITCZ) reflects in the latitudinal shifts of the currents. The variability of the

90 current strength appears as a regional response to the wind stress curl (WSC) distribution and

91 of the WSC strength over the basin (Johns et al., 1998; Fonseca et al., 2004; Garzoli et al., 2004,

92 Urbano et al., 2006; 2008). In the equatorial region, the EUC seasonal variability depends first

93 on the basin scale zonal pressure gradient, and also on the seasonal cycle of the local wind

94 forcing (Hisard and Hénin, 1987; Provost et al., 2004; Brandt et al., 2006; Hormann and Brandt,

95 2007; Brandt et al., 2016).

96 The interannual variability of the WTA boundary currents has been understudied because of

97 the lack of long-term data in this area. Nevertheless, Fonseca et al. (2004), using a combination

98 of altimetry and hydrographic data from 1993 to 2000, investigated the influence of the wind

99 on both the NBCR and the NECC variability. They did not find any direct relationship between

100 them. Hormann et al. (2012), used the surface velocity data derived from drifters between 1993

101 and 2009 and highlighted a relationship between the NECC intensity/location and the tropical

102 Atlantic climate modes (ACM), represented by positive and negative phases of the Atlantic

103 zonal mode (AZM) and the Atlantic meridional mode (AMM) (Cabos et al., 2019). They found

104 the intensity to be related to the cold phase of AZM and the core location to be related to the

105 warm phase of AMM. In the equatorial Atlantic, Hormann and Brandt (2007) also found such

106 relationship, using a high-resolution ocean general circulation model, observations and sea

107 surface temperature (SST) data. They showed that the EUC transport is affected by the cold and

108 warm events of the AZM (the so called "Atlantic Niño / Niña") and confirmed the previous

109 findings of Goes and Wainer (2003) concerning the link between the interannual variability of

110 the wind and the AZM impacting the strength of the tropical Atlantic circulation.

111 In this study, we propose to revisit the scheme of the WTA boundary surface circulation using

112 a 25-year time series of gridded altimeter-derived geostrophic currents. This dataset is longer

113 than the one used by Fonseca et al. (2004) and allows us to provide a more robust description

114 of the current branches described above, as well as of their seasonal and interannual variations.

115 The data also allows us to infer regional relationship among these currents. The paper is

116 organized as follows: in Sect. 2, the data and methods used are presented. Section 3 brings some

117 general characteristics of the current variability in the study area. In the fourth section we

118 analyze and discuss the seasonal and spatial variabilities of the surface geostrophic currents and

119 propose an updated seasonal map of the WTA surface circulation. The interannual variability

120 of the circulation is analyzed in Sect. 5. Section 6 is devoted to a general discussion, and Sect.

121 7 offers a summary and some perspectives.
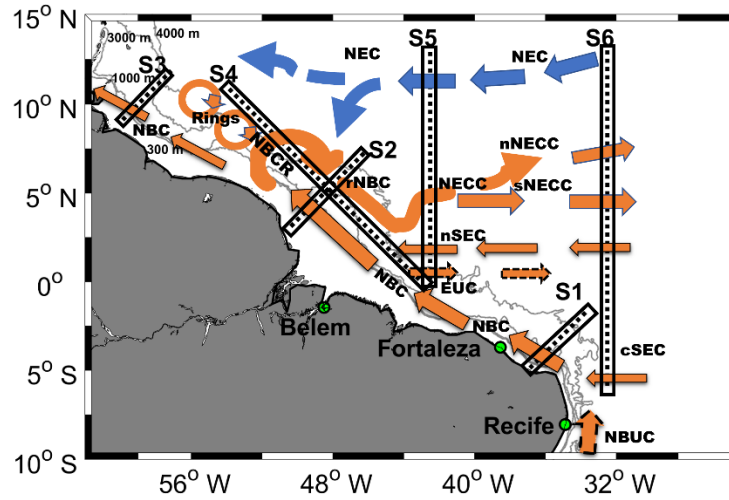
122

123

124

125

126

Figure 1. Schematic view of the western boundary surface circulation in the tropical Atlantic based on Schott et al. (2004), Goës et al. (2005), Urbano et al. (2006; 2008) and Aroucha et al. (2019). The distribution of the horizontal section used to study the different current branches are also indicated in black: S1, S2, S3, S4, S5 and S6. Solid and dashed arrows are the upper and the subsurface currents, respectively. The blue and orange colors of the arrows show connections with the northern and southern hemisphere waters, respectively. Acronyms are listed in Table 1. The 300 m, 1000 m, 3000 m and 4000 m isobaths (grey lines) are from the ETOPO2v1 database.

2 Data and methods

2.1 Altimeter-derived geostrophic currents

From along-track altimetry sea surface height measurements of all available satellite missions, the Copernicus Marine Environment Monitoring Service (CMEMS) produces daily maps of ocean dynamic topography, and derives then geostrophic surface currents. Here, we use the SEALEVEL_GLO_PHY_L4_REP_OBSERVATIONS_008_047 product (https://resources.marine.copernicus.eu) from January 1993 to December 2017. Daily maps of dynamic topography are estimated by optimal interpolation on $0.25° \times 0.25°$ global grid (details can be found in Pujol et al., 2016), and the geostrophic currents are computed using the 9-points stencil width methodology (Arbic et al., 2012) for latitudes outside the equatorial band (Equator $\pm5°$) and in the equatorial band, the currents have been calculated using the Lagerloef methodology (Lagerloef et al., 1999) which used the β-plane approximation as the Coriolis parameter vanishes close/at the equator.

Table 1. Acronyms and abbreviations

AMM	Atlantic Meridional Mode
AMOC	Atlantic Meridional Overturning Circulation
AZM	Atlantic Zonal Mode
EUC	Equatorial Undercurrent
ITCZ	Intertropical Convergence Zone
NBC	North Brazil Current
rNBC	Retroflected branch of the NBC
NBCR	North Brazil Current Retroflection
nNBCR	Northern NBCR flow
nNBCR lat	Latitude of the nNBCR maximum intensity
sNBCR	Southern NBCR flow
sNBCR lat	Latitude of the sNBCR maximum intensity
NECC	North Equatorial Countercurrent
nNECC	Northern branch of the NECC
nNECC lat	Latitude of the nNECC core
sNECC	Southern branch of the NECC
sNECC lat	Latitude of the sNECC core
PIRATA	Prediction and Research Moored Array in the Tropical Atlantic
SEC	South Equatorial Current
cSEC	Central branch ot the SEC
nSEC	Northern branch of the SEC
VnNBCR	Value of the nNBCR maximum speed
VsNBCR	Value of the sNBCR maximum speed
VnNECC	Value of the nNECC core speed
VsNECC	Value of the sNECC core speed
ESC	Equatorial Surface Current
WSC	Wind Stress Curl
WSC neg max	Maximum negative WSC
WSC strength	WSC strength
WTA	Western tropical Atlantic

For the present work, focusing on the seasonal and interannual variability, the daily gridded velocity fields from CMEMS have been averaged monthly. Note that, data with high variability (standard deviation > 0.4) have been removed. They are found in the Amazon region which is not a primary area of interest for this study, and where, the annual mean current speeds are unrealistic (higher than 2.5 m s^{-1}), probably due to geographically correlated errors (Pujol et al., 2016). We have then defined six horizontal sections (called S1, S2, S3, S4, S5 and S6, respectively), so that they cross perpendicularly at least one of the regional current branches (see Fig. 1). For each section, the original zonal and meridional surface velocity components have been rotated in order to derive the along-section and cross-section velocity components. In this study, we considered only the cross-section component, and the rotation angles considered for the oblique sections S1-S2-S3/S4 are 45°/315°.

To validate geostrophic current estimates in the equatorial region, we have compared them to the PIRATA current meter mooring data available in the study area (0°N, 35°W) over the 11/10/2017-29/01/2018 (Fig. 1 in the supplementary material). The data of the current meter

167 were obtained at 12-m depth and have been averaged each 5 days. The results of the comparison

168 with the geostrophic currents interpolated to the same location were in agreement with the

169 results of the previous studies in the equatorial Pacific (Picaut et al., 1989; Lagerloef et al.,

170 1999). However, all these studies the geostrophic currents are underestimated compared to the

171 observations, and this is because the contribution of the ageostrophic velocities has not been

172 considered (e.g. Fig. 1 in the supplement). The correlation of 0.71 is found on their zonal

173 components while the one on the meridional components is lower (<0.5) (Figure 1a-b in the

174 supplementary material). The mean biases/differences in standard deviation for both

175 components are respectively, 0.04/0.11 m s^{-1} and 0.14/0.03 m s^{-1}. The similar values were also

176 found by Lagerloef et al. (1999) in the western equatorial Pacific when comparing the

177 geostrophic currents to the current meter mooring data at 10-m depth. These results give credit

178 to the geostrophic estimates used in this work for the equatorial region even though their values

179 are underestimated compared to other observations (Picaut et al., 1989; Lagerloef et al., 1999,

180 Pujol et al., 2016).

181 **2.2 Wind velocity**

182 Monthly wind velocity fields from the ERA5 atmospheric reanalysis produced by the European

183 Centre for Medium-Range Weather Forecasts (ECMWF, http://www.ecmwf.int) are used in

184 order to evaluate the influence of the remote winds on the WTA ocean circulation. They were

185 downloaded from the Copernicus Climate Change data server over the January 1993 -

186 December 2017 period. We used the wind velocity data to calculate the wind stress field as

187 follows.

188 The zonal and meridional components of the wind stress, τ_x and τ_y are calculated using

189 empirical formulations (Large and Pond; 1981: Gill, 1982; Trenberth et al., 1990) following

190 NRSC (2013):

191 $$\tau_x = \rho_{air} C_D W * U \tag{1}$$

192 $$\tau_y = \rho_{air} C_D W * V \tag{2}$$

193 where U/V represent the zonal/meridional wind velocity components; W, the wind speed

194 amplitude; ρ_{air}, the air density (1.2 kg m^{-2}); C_D, the drag coefficient at the ocean surface,

195 calculated according to Large and Pond (1981).

196 The wind stress curl (WSC) is then deduced following Gill (1982):

197 $$Curl(\tau) = \frac{\partial \tau_y}{\partial x} - \frac{\partial \tau_x}{\partial y} \tag{3}$$

198

Over the tropical Atlantic, the ITCZ location has been determined from the WSC near-zero values. Then, the minimum/maximum of the negative/positive WSC values has been derived, and the WSC strength values (sum of the absolute minimum negative and maximum positive values) have been computed. Each of these parameters is zonally averaged over the region covering 6° S -16° N, and 30° W-0° E, following Fonseca et al. (2004).

2.3   Sea Surface temperature

Monthly estimates of Sea Surface temperature (SST) are also used in order to compute the Atlantic climate mode indexes and evaluate their possible relationship with the interannual changes observed in the WTA boundary circulation. A global gridded SST product, with a 1° spatial resolution is downloaded from the NOAA repository (https://www.esrl.noaa.gov/psd/data/gridded/data.noaa.oisst.v2.html, Reynolds et al. 2002). The AZM index is calculated considering the SST anomalies (SSTA) relative to the 1993-2017 monthly climatology in the ATL3 region bounded by 3° S-3° N/20° W-0° E (Zebiak, 1993, Hormann et al., 2012). The AMM index is also based on SSTA relative to the 1993-2017 monthly climatology, and calculated as the difference between the spatial average SSTA in the box 5° N-25° N/60° W-20° W and the spatial average SSTA in the box 20° S-5° N/30° W-10° E (Servain, 1991; Hormann et al., 2012).

3   General characteristics of the circulation in the Western Tropical Atlantic

The mean WTA surface geostrophic circulation is first derived by averaging the gridded altimetry current maps over 1993-2017 (Fig. 2a). We distinguish three different areas. From south/east to north/west:

1) The NBC formation area starting around 5°S: the westward cSEC flowing north of 6°S (mean value of ~ 0.3 m s^{-1}) feeds the NBC-NBUC current system around 34°-36° W. The NBC amplitude increases along its northward along-shelf course, up to 0.8 m s^{-1} around 3° S. Then it slows down toward the equator, before increasing again north of 3° N. Along the coast, farther north, its mean velocities are again weaker, with values of ~ 0.3 m s^{-1}.

2) The NBC retroflection region between 5°-8° N: in this area, the NBC undergoes an eastward recirculation, which feeds a southeastward current so-called the NBC retroflected branch (rNBC). The rNBC reaches annual mean velocities of ~0.6 m s^{-1}.

229   3) Between 3°-6° N and 42°-46° W, the rNBC meanders with an annual mean velocity of
230   0.5 m s^{-1} and partly feeds the surface eastward NECC which decays along its course.
231   This area is located in a region of high wind variability (Figure not shown).

232   In addition, we also observe the westward nSEC flowing between 2°-6° N, with stronger
233   velocity values at the eastern part of the basin (mean velocity larger than 0.3 m s^{-1}).

234   We computed the mean power spectral density of the daily geostrophic current time series in
235   order to detect the dominant components of the WTA current variations (not shown). It
236   highlighted three main energy zones:

237   1) at intraseasonal timescales with different peaks at periods less than 120 days,

238   2) at seasonal timescale,

239   3) at interannual timescale, with peaks at periods larger than 600 days.

240   We then filtered the velocity time series using different cutoff frequencies in order to isolate
241   each of this component of the current variability: below 120 days, between 120 days and 600
242   days and above 600 days. We computed the ratio between the standard deviation of each filtered
243   current field and of the total current field. The resulting maps (Fig. 2b-d) show the relative
244   importance of each component with regard to the total variance, as a function of the location.
245   We observe the predominance of the seasonal variability in the whole WTA (overall ratio of
246   0.44), with the highest values (0.48) observed along the continental shelf, in the NBC region,
247   and between 0°-2° S east of 36° W. Intraseasonal fluctuations are also important in the same
248   areas (with the largest ratio of 0.44) while the interannual variability is weaker with the highest
249   values (>0.2) observed in the NECC area north/east of 4° N/40° W (consistent with Richardson
250   and Walsh, 1986). In this study, we focus on the seasonal and interannual timescales.
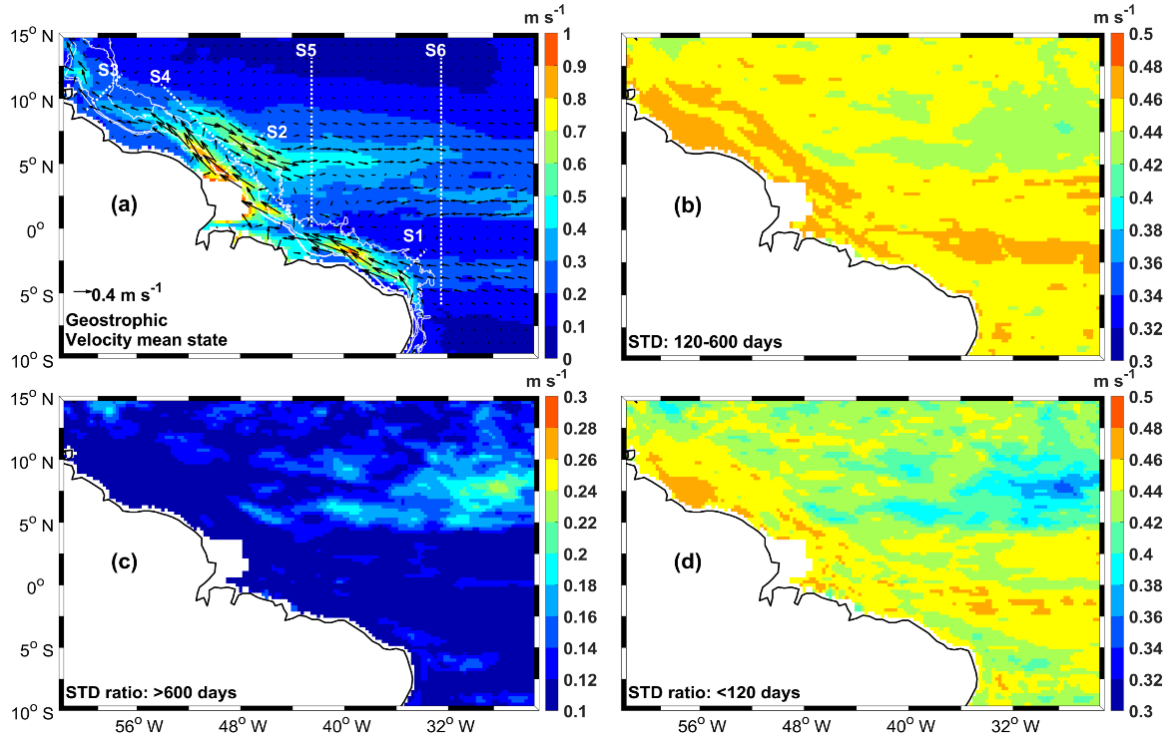
251

Figure 2. (a) Temporal mean of the geostrophic currents (amplitude in m s^{-1} and vectors) in the study area between 1993 to 2017; **(b), (c)** and **(d)** ratios between the standard deviations of the currents for the signals between 120 and 600 days, longer than 600 days and shorter than 120days, respectively, and the standard deviation of the total currents. The white dashed lines S1, S2, S3, S4, S5, S6 in **(a)** represent the cross-sections of the currents, and the solid white lines are the 300 m, 1000 m, 3000 m and 4000 m isobaths. Note that, the colobar of **(c)** is different than the ones of (b) and (d).

To further investigate the variability of the different current branches, we then monthly averaged the daily geostrophic currents and extracted the cross-section geostrophic velocities along the six sections defined above (Fig. 1). In order to remove the intraseasonal variability, the monthly velocity estimates are further low-pass filtered using a 4-month cutoff frequency. The time-space diagrams (also called Hovmöller diagrams) along the six sections are plotted in Fig. 3. We can clearly observe large changes in both time and space with respect to the different current branches, illustrating the complexity of the surface circulation in the WTA. The seasonal and, in a lesser extent, the interannual current fluctuations mentioned above are clearly visible in the different sections. For each of them, the time-average current values are also computed as a function of the latitude (left-side plots in Fig. 3), highlighting the mean spatial extension of the current paths crossing the corresponding section. Note that in addition to the main currents mentioned in Fig. 1, between 2° S-2° N, the sections 4 to 6 show an eastward surface current, located at the same location of the EUC, west of 44°W along the equator (Schott

273   et al., 1998). Depending on the season the EUC core is known to be located between about 100-

274   m depth and 50-m depth (Brandt et al., 2016). At 44° W, Bourlès et al. (1999b) have also noticed

275   the presence of an eastward surface flow above the EUC, which was identified to be different

276   than the EUC. The presence of this eastward surface flow is also confirmed by the PIRATA

277   current meter data available in our study area (0-35°W: see Fig. 1 in supplementary material,

278   from November 2018 to March 2019). These findings motivate our investigation of the

279   variability of the surface currents in the equatorial part of our study area. We chose to name

280   this eastward surface flow the Equatorial Surface Current (ESC) hereinafter in order to further

281   investigate this signal also captured in our sections 4, 5 and 5.

282   Table 2 summarizes the mean current width derived along the different sections (using left-side

283   plots in Fig. 3). Note first that a positive current convention is chosen for the sections as follows:

284   northward NBC along sections 1 to 3; eastward NBCR along section 4; eastward NECC along

285   sections 5 and 6, and eastward ESC along sections 4 to 6. Hence, the signatures of the rNBC

286   on the section 2, the nSEC (sections 4 to 6) and the cSEC (section 6) are considered as negative.

287   From Table 2, we observe that the NBC becomes narrower from the section 1 to the section 2.

288   The retroflection zone (section S4, Fig. 3S4) extends from 3.7° N to 10.5° N, in agreement with

289   Fonseca et al., (2004) who found the northernmost position of the NBCR around 11° N. North

290   of the retroflection, the NBC along the Guyana coast is weaker, but broader relatively to the

291   section 2 (NBC2 and NBC3 in Fig. 3). From section 6 to 4, the nSEC signature changes. It is

292   wider at 32° W (nSEC6), then narrower at 42° W (nSEC5), and widens again closer to the shelf

293   at 44° W (nSEC4) (respectively 550, 67 and 190 km in Table 2). The NECC extension also

294   varies from 32° W to 42° W, and is wider and located further north on the east, with a mean

295   width extending from 860 km (NECC5) to 920 km (NECC6).

296

297

298

299

300

301

302

Table 2. Extension in latitude and km of the different currents branches crossing the different sections: NBC1, NBC2 and NBC3 are respectively the North Brazil Current captured on sections 1, 2 and 3; NECC5 and NECC6 are respectively the North Equatorial Countercurrent on the sections 5 and 6; nSEC4, nSEC5 and nSEC6 are respectively the northern branch of the South Equatorial Current (SEC) on the sections 4, 5 and 6; cSEC6 is the central branch of the SEC on the section 6; and ESC4, ESC5 and ESC6 are the Eastward Equatorial Surface Current on respectively on the sections 4, 5 and 6.

List of current paths	Latitudinal coverage	Current width (km)
NBC1	1.3° S-4.6° S	~ 520
NBC2	3.6° N-5° N	~ 220
rNBC2	5° N-7.4° N	~ 380
NBC3	9.1° N-11.9° N	~ 440
NBCR4	3.7° N-10.5° N	~ 760
nSEC4	2° N-3.7° N	~ 190
ESC4	1.2° N-2° N	~ 120
NECC5	2.4° N-10.1° N	~ 860
nSEC5	1.7° N-2.3° N	~ 70
ESC5	0° N-1.7° N	~ 190
NECC6	4.1° N-12.4° N	~ 920
nSEC6	0° N-4.1° N	~ 550
ESC6	0° S-1.4° S	~ 110
cSEC6	1.4° S-5.9° S	~ 500
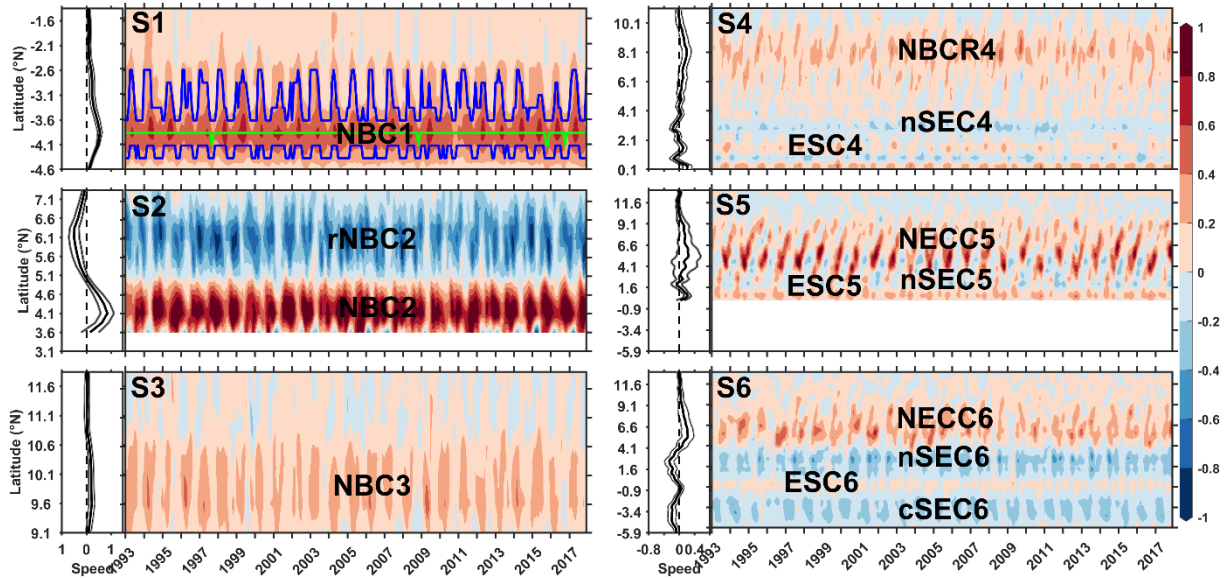
Figure 3. Hovmöller diagrams (1993 to 2017) of the cross-section current components (m s^{-1}) for S1, S2, S3 S4 S5 and S6. On the left of each panel, the time average over the section is shown (thick lines), framed by the corresponding standard deviation (thin lines). The color shading shows the northward/eastward (red) or southward/westward (blue) direction of the cross-current. Acronyms are listed in Table 1. The numbers next to the acronyms represents the number of the section. The green line in S1 indicates the time series of the maximum velocity of the cross-section current (NBC), and is framed by the time series of the maximum velocities divided by 2 (blue lines) over 1993-2017 period.

319 In order to further investigate the temporal variations of the current strength, the maximum
320 speed values of each current path have been determined for each month. The maximum speed
321 corresponds to the current core velocity and is called Vmax hereafter: (see Fig. 3, green line on
322 S1). The location of the core velocity is also computed. Then, to estimate the current relative
323 strength/intensity, we have considered the part of the sections of velocities larger than Vmax/2
324 (see Fig. 3, blue lines on S1), and we finally computed the values by averaging the velocity
325 values over the area where $V\_max/2 < V < V\_max$. The width of the currents (Table 2) is
326 determined by the average velocity value over the whole period of study (1993-2017) (see left
327 boxes of the Hovmöller diagrams of Fig. 3). Then, knowing the sign or direction of the current
328 (eastward or westward), the zero-contours of the velocity fields are used to define the width of
329 the currents. Note that the current strength/intensity has also been computed by averaging
330 velocity values over the entire width of the current paths (e.g., not only where the velocity is
331 larger than Vmax/2), but the results did not correctly reflect the current variability observed in
332 Fig. 3 and Fig. 4 (not shown).

333 For the NBCR and the NECC, the variability of the maximum speed of the apparently two
334 flow/branches and their corresponding locations is also analyzed, in order to compare the result
335 with the study of Fonseca et al. (2004). The goal is also to investigate the variability of the
336 current location with respect to the wind variability and to the tropical Atlantic climate modes.
337 In this study, the presence of two flows of the NBCR and the NECC two-core structure are
338 identified when the velocity profile shows two local maxima separated by a local minimum
339 respectively, in the NBCR region (considered between 4°-10° N) and the NECC region
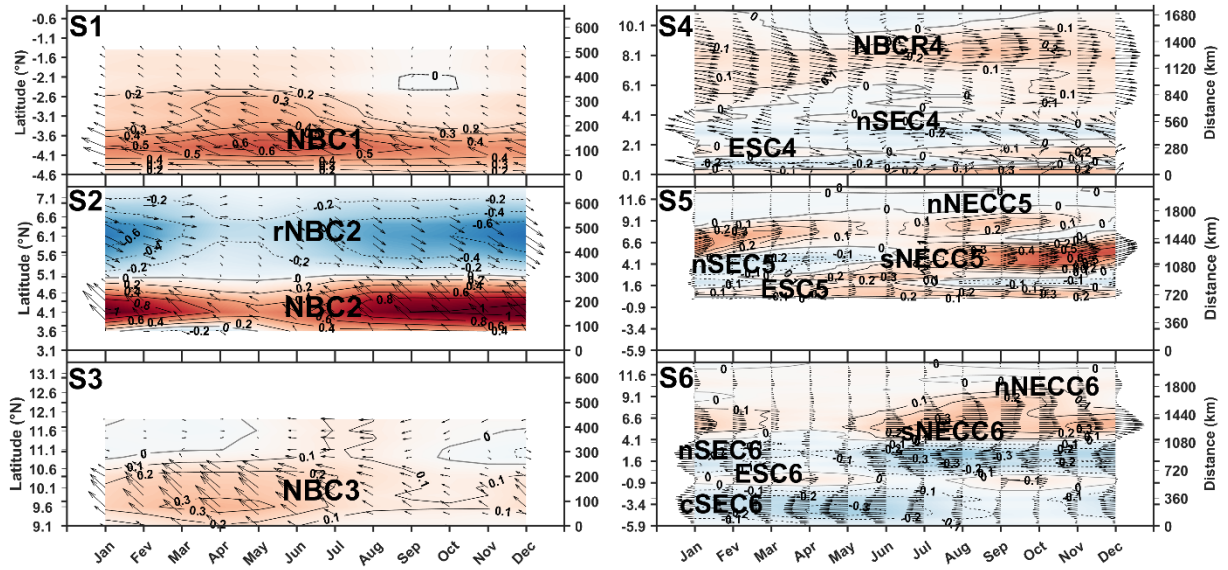340 (considered between 3°-11° N) (Fig. 4S4-S6).

341

342

Figure 4. Average seasonal cycle obtained from Figure 3 (vectors of the currents are superimposed on the contour of their amplitude in m s^{-1}). On the right side of each subplot, the distances from the southernmost point (in km) are indicated.

4 Seasonal variability

Here we focus on the seasonal cycle of the different current branches observed in the study area. Therefore, a monthly climatology of the velocity estimates shown in Fig. 3 is calculated for each of the six sections (Fig. 4). For further analysis, the monthly climatology of Vmax, Vmax location and the relative current intensity has also been derived from the corresponding monthly time series for different current components (Fig. 5).
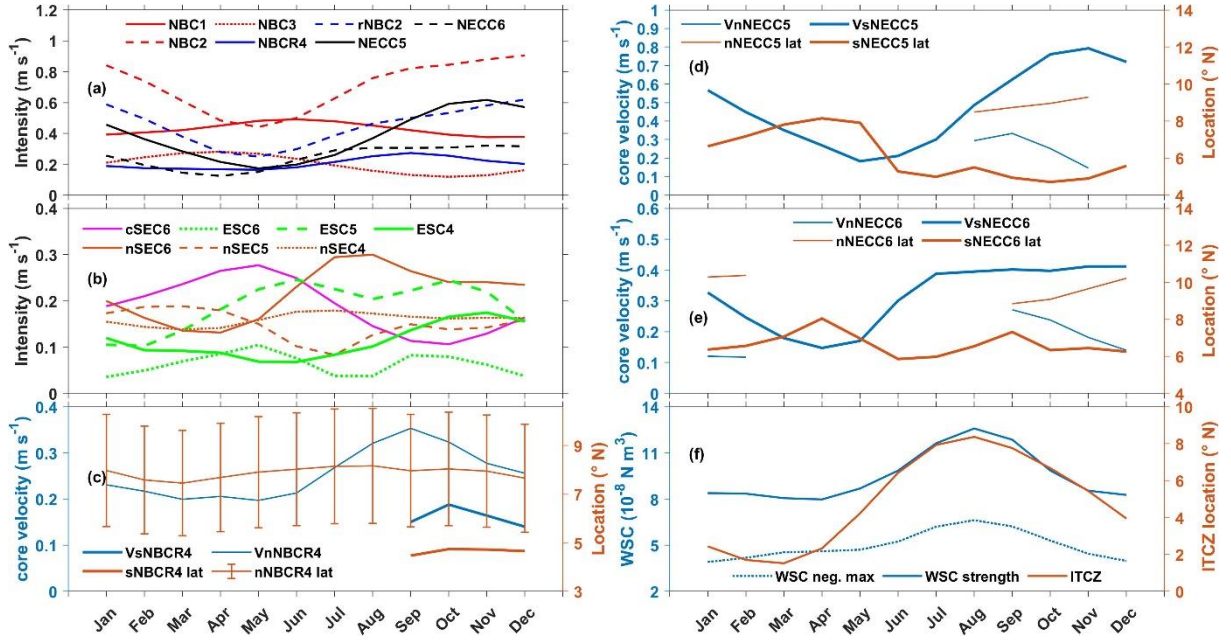
Figure 5. Monthly climatology of: the relative currents' speed (m s^{-1}) **(a-b)**; the cores velocity/location in the NBCR regions **(c)**; the core velocity/location of the NECC branches along sections 5 and 6 **(d-e)**; and the absolute values of the maximum negative wind stress curl (WSC neg. max), the WSC strength and the ITCZ location **(f)**. Acronyms are listed in Table 1 and the numbers next to the acronyms represents the number of the sections. On **(c)**, **(d)** and **(e)**, the core velocities and locations are respectively, in blue and orange color.

4.1   The North Brazil Current and its retroflection

In Fig. 4, the NBC (Section 1) and the cSEC (Section 6) are both observed located at ~ 4° S and present similar seasonal cycles, with stronger flows during the first half of the year. The cSEC6 velocity maximum (0.3 m s^{-1}) / minimum (0.1 m s^{-1}) appears in May/October, respectively. The NBC1 velocity maximum (0.6 m s^{-1}) / minimum (0.4 m s^{-1}) appears in May-June/November-December (Fig. 5a). These annual cycles are also similar to the annual cycle of the NBUC transport observed by Rodrigues et al. (2007) at 10° S and which is related to the bifurcation location of the sSEC. This suggests that at its southernmost location, the seasonal variability of the NBC might be partly driven by the location of the sSEC bifurcation, which has been shown to be influenced by the annual cycle of the WSC over the area 5°–10° S, 25°–40° W (Rodrigues et al., 2007).

When comparing the NBC along sections S1, S2, S3 and S4 (Fig. 4S1-S4 and Fig. 5), it clearly depicts two different seasonal cycles along its northward path. The NBC2, NBCR4 and the rNBC2 flows show approximately the same seasonal cycles, in opposite phase with NBC1 and NBC3 ones. NBC2 is narrower but relatively stronger than NBC1. It decreases from January to May (by ~ 0.4 m s^{-1}), and then increases again to reach a maximum in November-December (1 m s^{-1}). Compared to NBC2, the rNBC2 is broader (width of ~ 350 km against 200 km) but less

15

379   intense (maximum of 0.6 m s^{-1} in November-December). Apparently, the NBC2 width and

380   strength seem to be linked to the nSEC intensity in the eastern basin (see nSEC6 and nSEC4 in

381   Fig. 5b). When the nSEC is weaker, the NBC2 is also weaker and narrower. Then, the NBC2

382   intensifies one month later when the nSEC intensity is increasing. This shows the importance

383   of the nSEC contribution to the NBC in the northern hemisphere. The delay between the nSEC

384   and NBC2 growth can be due to the mesoscale activities more intense in the western basin

385   (Aguedjou et al., 2019). The fact that the NBC1 and the NBC3 are in phase when the nSEC

386   contribution to the NBC2 is lower might also indicate that the NBC is more stable when the

387   intrusion of water from the nSEC is weak. The latter may generate barotropic and baroclinic

388   instabilities of the NBC which then tends to retroflect eastward. This could explain the phasing

389   of the annual cycle of the NBC2, NBC4 and rNBC2.

390   In Fig. 4, from September to January, we observe two retroflections of the NBC: the main one

391   around 8°N and a secondary one more to the south, between 4-6° N (Fig. 4S4 and 5c). The flow

392   of this secondary retroflection (called sNBCR) reaches its maximum intensity in October while

393   the main retroflection flow (called nNBCR) reaches its maximum one month earlier. Then, it

394   migrates northward to join the nNBCR4; and both are completely merged at the beginning of

395   the following year (Fig. 4S4). Both branches merge at the beginning of the year and the NBCR

396   then weakens to reach its minimum intensity in May. Note that the seasonal cycles of the NBC2

397   and of the NBCR are similar to the one of the NBC transport obtained by Johns et al. (1998)

398   and Garzoli et al. (2004) using acoustic Doppler current profilers (ADCP)/Inverted Echos

399   sounders/Pressure gauge data. Johns et al. (1998) related the seasonal cycle of the NBC

400   observed in this area to the remote wind stress curl forcing across the tropical Atlantic. Here,

401   we also see that the seasonal cycles of the NBC branches north of the equator (except the NBC

402   continuity along the Guyana coast) seem to follow the remote wind stress curl strength with a

403   delay of one to four months (Fig. 5a-f). The latter should be impacted by the mesoscale activities

404   and/or wave propagations in the region (Fonseca et al., 2004). The northernmost location of the

405   nNBCR maximum intensity occurs in August, when the maximum WSC strength is reached

406   (Fig. 5c, f). The root mean square (rms) of the monthly mean values of its location (Fig. 5c) is

407   nearly constant (~2.3°), and is consistent with the fact that there may not be a preferred season

408   for NBC ring formation (Garzoli et al., 2003; Goni and Johns, 2003). Indeed, Garzoli et al.

409   (2003) have shown using inverted echo sounder observations that there was a link between the

410   rapid northward/southward extension of the NBC retroflection and the shedding of the rings in

411   this region.

412 Farther north, the NBC component flowing along the Guyana coast (NBC3) is twice wider (~

413 440 km) and less intense than the NBC2 (Fig. 4S2-S3). It reaches a minimum in October (~ 0.1

414 m s^{-1}), and a maximum during March-May (0.3 m s^{-1}) when the NBCR4 is minimum (Fig. 4S3-

415 S4 and 5). As already mentioned, its seasonal cycle is similar to the NBC1 and cSEC, and might

416 also be influenced by the sSEC bifurcation location.

4.2   The North Equatorial CounterCurrent

418 The NECC (both NECC5 and NECC6) seasonal cycle is similar to the ones of the NBC2,

419 NBCR4 and rNBC2 (Fig. 4S2, S4, S5-S6). It weakens along its pathway and its intensity is

420 maximum in November-December (~ 0.6 m s^{-1} at 42° W and ~ 0.3 m s^{-1} at 32° W), and

421 minimum in April-May (Fig. 5a).

422 During the second part of the year, we observe the two-core structure previously investigated

423 by Urbano et al. (2006; 2008). The two cores/branches are seen first at 42° W in August, then

424 at 32° W in September (Fig. 4 and 5d-e). The northern branch (nNECC) is narrower (between

425 7°-9° N) and stronger (0.3 m s^{-1}) in August-September at 42° W (Fig. 4S5 and 5d). It is even

426 separated from the southern branch from October to December. At 32° W, the northern

427 core/branch is stronger from September (northern core velocity of ~ 0.2 m s^{-1}) to November. It

428 is gradually decreasing in intensity and shifting northward until forming a separated second

429 branch, located between 9-11° N from December to February, and then becomes very weak in

430 March-April (Fig. 4S5 and 5e).

431 From June to July, the NECC signature (sNECC branch) is located between 3-4° N at 42° W,

432 and is connected from the south to the eastward flow associated with ESC5 in Fig. 4S5. Urbano

433 et al. (2008) showed with ADCP data at 38° W that the eastward NECC cycle may start in this

434 region when the EUC is shallower and further north, and seems to be connected also to a

435 shallower NEUC during this period of the year. The presence of ESC5 suggests that it may be

436 the one that favors the surfacing and the connection of both currents during June-July. From

437 June to November, the sNECC branch increases simultaneously with the rNBCR2. However, it

438 reaches its maximum one month earlier (November) and starts decreasing when the rNBC is

439 still increasing. This confirms that the NECC is not only fed by the rNBC at the surface as

440 suggested by Verdy and Jochum, 2005. The sNECC witnesses the same variability at both 32°

441 W and 42° W, but reaches its minimum early in March-April at 32° W when the climatological

442 NECC is described in the literature as a reversing flow or is missing at its usual location (Garzoli

443 and Katz, 1983; Garzoli, 1992). At this location (32° W), the sNECC starts increasing from

444 April-May, between 4°-6° N far from the ESC, and grows until November. Burmeister et al.

445   (2019) showed that, in the central Atlantic, when the ITCZ migrates northward (April to

446   August) (Fig. 5f), the nSEC recirculates eastward to reach the NEUC which then increases. The

447   presence of the sNECC flow in April-May may suggest that the NECC flow might be initiated

448   by an eastward recirculation of the nSEC which flows on top of the NEUC during this period.

449   It reaches its first maximum in July-August together with the nSEC, and a second maximum in

450   November (Fig. 5a, b, e).

451   At 32° W and 42° W the sNECC shows two northward migrations. The first one occurs from

452   June-July (June) to August (September) at 42° W (32° W), and the second one from October to

453   April (Fig. 5d-e). Fonseca et al. (2004) also found such behaviors but with some differences:

454   two northernmost NECC locations in February and August, and two southernmost NECC

455   locations in June and December. But they lacked data between March and May, and we do not

456   use the same methods to compute the core position.

457   4.3   The central and northern branches of the South Equatorial Current

458   The cSEC and nSEC which are two branches of the westward SEC do not have the same

459   seasonal cycle (Fig. 4S4, S5, S6). This is due to the fact that, in the northern hemisphere, the

460   nSEC can be affected by the Southeast Trades which cross the equator. However, the nSEC4,

461   nSEC5 and nSEC6 have maxima at different periods of time. At 32° W, the nSEC (nSEC6)

462   increases from April to reach a maximum of ~ 0.3 m s^{-1} in August, following the migration of

463   the ITCZ (Fig. 5b, f). During this time, at 42° W, the nSEC (nSEC5) migrates northward, and

464   its intensity decreases until July, when it almost disappears. The ESC then appears (Fig. 4S5).

465   The nSEC5 is observed again after July, increases and reach a maximum of ~ 0.2 m s^{-1} in March

466   (Fig. 4S5, S6 and Fig. 5b). Over the continental shelf, most of the nSEC joins the NBC (section

467   4, around 2-4° N and 46° W) and a part deviates southeastward to join the rNBC and form the

468   eastward ESC4 (captured along section 4, Fig.4S4). The nSEC component that joins the NBC

469   reaches its maximum of ~ 0.2 m s^{-1} between June and August (also following the ITCZ

470   northward migration, Fig. 5b, f). However, the nSEC seasonal variations are relatively small (~

471   0.15 m s^{-1}) (Fig. 4S4). It is particularly true for nSEC4 but the angle of the section relative to

472   the flow probably leads to a significant reduction of the current amplitude captured.

473   4.4   The Equatorial Surface Current ESC

474   Figure 4S4-S6 show the presence of an eastward current near the equator. Such feature was

475   already observed and mentioned by Hisard and Hénin (1987) and Bourles et al. (1999b) using

476   hydrographic and ADCP data. In Fig. 4S4, eastward flows are captured between 1-2° N (ESC4)

477 and along the equator. As mentioned in Sect. 4.3, they may be composed of the part of the nSEC

478 that does not join the NBC and the rNBC (which is known to feed the EUC in the thermocline

479 layer). The weaker intensity of ESC4, compared to ESC5 (i.e. ESC at 42) is explained by the

480 angle between S4 and the current direction. But the weaker intensity of ESC6 (i.e. ESC at 32°

481 W) is due to the weakening of the corresponding eastward flow between both longitudes. ESC4

482 and ESC5 are observed almost throughout the year (Fig. 4S4-S6) and their amplitude follows a

483 semi-annual cycle (Fig. 5b) similar to the EUC in the eastern Atlantic (Hormann et al. 2007).

484 However, the periods of the maxima are slightly different from one location to the other. ESC4

485 semi-annual cycle shows a weak maximum in March-April (~ 0.1 m s^{-1}) and another maximum

486 in November (~ 0.2 m s^{-1}). ESC5 amplitude is larger because of the merging of ESC4 with the

487 eastward flow observed along the equator (Fig. 4S5). Its maxima occur in June and October

488 with similar intensities (more than 0.2 m s^{-1}) (Fig. 5b). ESC6 (at 32° W) is weaker, but reaches

489 its maxima in May and in September-October (less than 0.1 m s^{-1}). Since this eastward ESC

490 current component is almost not documented in the literature, we will further discuss it in Sect.

491 6. Note that as mentioned in section 2.1, the ESC amplitude captured in the altimetry product

492 here is probably underestimated compared to the observations.

5   Interannual variability

494 Beyond the dominant seasonal variability of the circulation at regional scale, we also observe a

495 year-to-year variability of the surface velocities in the study area (Fig. 2 and Fig. 3). The latter

496 is analyzed here, using the time series of the characteristics (intensity and core velocity/location,

497 See Sect. 3) of the different current branches captured along the 6 sections (Fig. 6). We will

498 also analyze this variability in the light of the tropical Atlantic climate modes.

499 In Fig. 6a-b we observe that over the whole study period the intensities of the cSEC6 (cSEC

500 along section 6) and of the NBC1 (NBC along section 1) and NBC2 (NBC along section 2)

501 vary between 0.05-0.35 m s^{-1}, 0.3-0.6 m s^{-1} and 0.2-1.2 m s^{-1}, respectively. with corresponding

502 mean values of 0.2 m s^{-1} ± 0.06, 0.4 m s^{-1} ± 0.06 and 0.7 m s^{-1} ± 0.2. To the north, when crossing

503 section 3, the NBC weakens and ranges between 0.05-0.43 m s^{-1} with a mean intensity of 0.2

504 m s^{-1} ± 0.07. In the equatorial region (±5° of latitude), along sections 5/6, the nSEC intensity

505 varies between 0.05-0.3 m s^{-1}/0.1-0.4 m s^{-1}, with a mean value of 0.15 m s^{-1} ± 0.05/0.2 m s^{-1} ±

506 0.07 (Fig. 6b). The ESC intensity varies between 0.15-0.3 m s^{-1}, 0.05-0.4 m s^{-1} and 0-0.15 m s^{-1}

507 ^{1} when crossing sections 4, 5 and 6, respectively, with corresponding mean values of 0.12 m s^{-1}

508 ^{1} ± 0.05, 0.2 m s^{-1} ± 0.07, and 0.06 m s^{-1} ± 0.03.
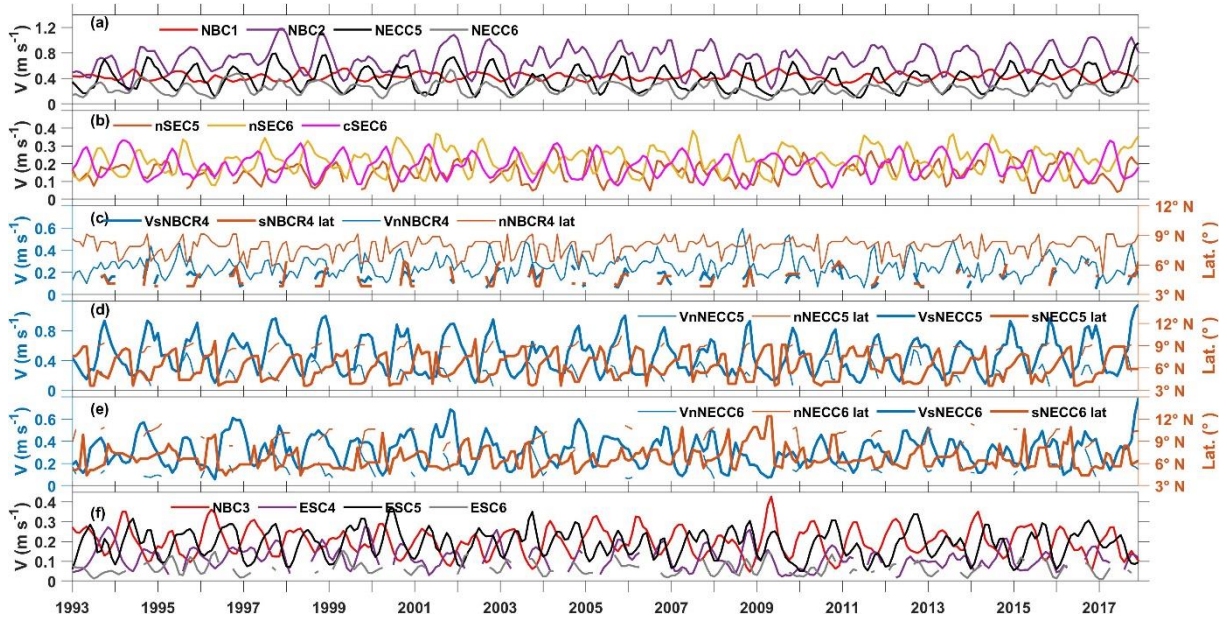
509

Figure 6. Time series of the 4-month low-pass filtered characteristics of the geostrophic currents **(a-f)** captured along sections 1 to 6. Acronyms are listed in Table 1 and the numbers next to the acronyms represents the number of the sections **(a)**: intensity of NBC1 and NBC2, and of the NECC5 and NECC6. **(b)**: intensity of the cSEC6 and of the nSEC5 and nSEC6. **(c)**, **(d)** and **(e)** core velocities and the locations of respectively the nNBCR4 and the sNBCR4 flows, the nNECC5, the sNECC5, the nNECC6 and the sNECC6. **(f)** Intensity of the NBC3, ESC4, ESC5 and ESC6.

The two-core structure of the NECC and the NBCR regions show the highest year-to-year variations in both velocity and location (Fig. 6c-e). The NECC/NBCR intensity and core velocity were found significantly correlated (>0.98) (sNECC and nNBCR; figure not shown). At 42° W, the sNECC/nNECC) velocity cores vary between 0.1-1.2 m s^{-1}/0.05-0.55 m s^{-1}, with mean values of 0.5 m s^{-1} ± 0.25/0.25 m s^{-1} ± 0.1. They are located between 3.6°-9.9° N/7.6°-10.4° N, with mean locations at 6.1° N ± 1.7°/8.9° N ± 0.8° (Fig. 6d). At 32° W, the cores vary between 0.05-0.8 m s^{-1}/0.05-0.5 m s^{-1}, with mean velocities of 0.3 m s^{-1} ± 0.13/0.2 m s^{-1} ± 0.09. They are located between 4.1°-12.4° N/7.4°-11.6° N, with mean locations of 6.6° N ± 1.4°/9.7° N ± 1.1° (Fig. 7e). The sNBCR/nNBCR maximum speeds crossing the section 4 varies between 0.05-0.3 m s^{-1}/0.05-0.6 m s^{-1}, with mean values of ~ 0.15 m s^{-1} ± 0.06/0.25 m s^{-1} ± 0.08. They are located between 3.9°-6.4° N/5.1°-9.1° N, with mean locations of 4.7° N ± 0.8°/7.9° N ± 0.8°. Northeast of the equator, for all these current branches, we observe important year-to-year variations, both in terms of current core location and of velocity amplitude.

For further analysis, the anomalies of the current's characteristics (intensity and core value/location) relative to their monthly climatology have been computed (Fig. 7). First, we do not see obvious relationships between the different resulting monthly anomaly time series over the whole period investigated. No relationship was found between the intensity of the NECC branches or of the NBCR flows and their location. However, for some particular years, both the NECC intensity/core velocity and location show significant anomalies at 32° W. For example, the monthly anomalies of the sNECC6 location were shifted far to the north (south) in 2009 and 2010 (1996 and 2001). Simultaneously, the monthly anomalies of the sNECC6 intensity/core value were unusually weak/strong (Fig. 7f-g).

To investigate the relationship between the AMM, the AZM, and the year-to-year variability of the characteristics of the different currents over 1993-2017 period, we computed the three-month rolling average of the time series of the current anomalies and of the climate mode indexes (so-called 3-month anomaly time series). So, the AMM and AZM peak events (respectively, March-April-May and June-July-August) have been correlated with the 3-month anomaly time series of the currents in order to learn more about their possible relationship at the interannual timescale in the study area (figures not shown). Only the correlations greater than ±0.5 and which have been found significant with 95 % of confidence level, performing the Student's t-test are discussed below (listed in Table 3).
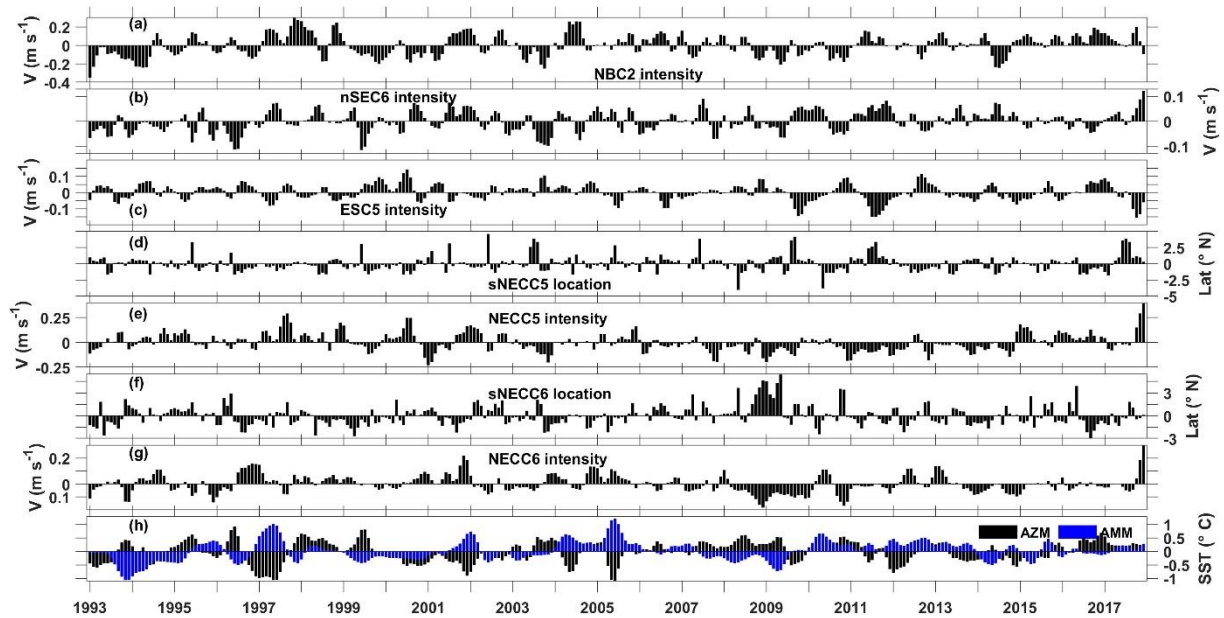

Figure 7. Time series of monthly anomalies relative to the monthly climatology for: **(a)**, the NBC2 intensity; **(b)**, the nSEC6 intensity; **(c)**, the equatorial surface eastward flow ESC5 intensity; **(d)**, the sNECC5 core location; **(e)**, the NECC5 intensity; **(f)**, the sNECC6 core location; and **(g),** the NECC6 intensity; **(h),** Normalized indexes of the AMM (blue color) and AZM (black color).

21

554 **Table 3.** Correlations values between the characteristics of the current branches and the Atlantic meridional and
555 zonal mode indexes (AMM and AZM, respectively). Where the correlations are found lower than 0.5, we indicate
556 "insignificant" over the whole time period ("none" for no month is related to this correlation). The current branches
557 analyzed are the NBC, the sNECC, the nSEC and the ESC.

Current branches' characteristics		Atlantic meridional mode (AMM) during March-April-May	Atlantic Zonal mode (AZM) during June-July-August
NBC1 intensity (section 1)	Correlation	Higher than -0.51	Insignificant
	Period	June-July	None
NBC2 intensity (section 1)	Correlation	0.58	Insignificant
	Period	March-April-May	None
sNECC5 intensity (section 5)	Correlation	Insignificant	-0.51
	Period	None	September
sNECC6 intensity (section 6)	Correlation	Higher than 0.50	Insignificant
	Period	March-April-May	None
sNECC6 core location (section 6)	Correlation	Higher than 0.51	Insignificant
	Period	March-April-May	None
nNECC6 core location (section 6)	Correlation	-0.62	Insignificant
	Period	March	None
nSEC5 intensity (section 5)	Correlation	Insignificant	-0.52
	Period	None	November
nSEC6 intensity (section 6)	Correlation	Higher than 0.52	Insignificant
	Period	March-April-May	None
ESC intensity (Sections 4 and 5)	Correlation	Higher than -0.55	Insignificant
	Period	May-June	None
ESC intensity (Section 6)	Correlation	Higher than 0.62	Higher than -0.52
	Period	March-April-May	June-July

558

559 The AMM index is found anticorrelated with the NBC intensity along the section 1 during
560 March-April-May, the nNECC core location along the section 6 and the ESC intensity west of
561 42° W, with respective coefficient of correlation (cc) higher than -0.51 during June-July, about
562 -0.62 in March, and higher than -0.55 in May-June. These anti-correlations show the probability
563 of the positive (negative) AMM phases to lead the negative (positive) anomalies of the nNECC
564 core location at 32° W with 0-month delay, the negative (positive) NBC intensity between 3°-
565 5° S and the ESC intensity anomalies (west of 42° W) with 1- to 2-month and 0- to 1-month
566 delay, respectively. However, the AMM index during March-April-May is found correlated
567 with the NBC intensity north of the equator before the retroflection (cc ~0.58) and, the sNECC
568 intensity/core location and the nSEC intensity at 32° W (cc higher than 0.50/0.51 and cc higher

than 0.52, respectively) during the same period of time. This suggests that the positive (negative) AMM phases probably drives the positive (negative) anomalies of the corresponding currents with no time lag.

During June-July-August, the AZM index is found anticorrelated with the sNECC/nSEC intensity at 42° W (cc=-0.51/-0.52) only in September/November. This suggests that the positive (negative) AZM phases probably lead the negative (positive) anomalies of the sNECC/nSEC intensity with 1- and 3-month delay, respectively.

The eastward ESC intensity at 32° W is found simultaneously correlated with AZM and AMM in June-July and March-April-May, with cc higher/lower than 0.62 and -0.52, respectively. This suggests that the positive (negative) anomalies of ESC at 32° W might be associated with both positive (negative) AZM and negative (positive) AMM phases with no delay.

Referring to Cabos et al. (2019), the relationships found between the currents and the AMM show the influence of the strengthening of the southeast trade winds on the southward migration of the nNECC core at 32° W, whereas the NBC intensity between 3°-5° S and the ESC intensity west of 42° W decrease, and vice versa. Conversely, the strengthening of the southeast trade winds may influence the northward migration of the sNECC core at 32° W, whereas the NBC2, sNECC6 and nSEC6 intensities increase, and vice versa. Referring to the same authors, the relationship with the AZM indicates the probable influence of the positive westerlies winds anomalies in the western part of the basin on the negative anomalies of the sNECC and nSEC intensities at 42° W, and vice versa. Concerning the ESC at 32° W the relationship with both the AZM and the AMM modes indicate its strengthening during the concurrent events of positive westerlies winds anomalies in the western part of the basin and the negative southerlies winds anomalies, and vice versa.

6   Discussion

Finally, we have computed the seasonal maps of the geostrophic currents in the whole WTA (Fig. 8) in order to have a regional view of the seasonal variations of the circulation. Fig. 8 confirms the results obtained from the analysis of the cross-section velocities in Sect. 4 (in terms of seasonal cycles and spatial structure) but also highlights interesting new features.

A large cyclonic circulation is observed between 35°-45° W and 0°-5° N during boreal spring (blue ellipse). The latter is formed by the westward nSEC which is suddenly deviated to the northeast by the presence of the ESC at ~32° W. Then, near 44° W and 5° N, the nSEC meets

the rNBC which reaches it southernmost position during this season, and deviates to the southeast. When reaching the equatorial region between 0°-2° N, where the ESC is found (Fig. 4), the resulting flow becomes stronger, and is deviated to the east, close this cyclonic feature. This finding might answer the question of Schott et al. (1998) about the destination of the rNBC during spring, when the rNBC does not feed the NECC anymore. From German cruises SADCP measurements (downloaded from the data center PANGEA https://doi.pangaea.de/10.1594/PANGAEA.937809 and described in Tuchen et al, 2022), the zonal and meridional components of currents over the equatorial region have been analyzed (40°W, 35°W and 32°W: figures in supplementary material). They confirm the existence of the eastward ESC, with a shifting tendency to the north at 35°W. During the boreal winter, another cyclonic circulation is observed between 44°-50° W and 5°-10° N (blue ellipse in Fig. 8): part of the NECC recirculates north-westward to join the rNBC. During both boreal winter and spring, south-westward recirculations of the NECC appear to strengthen the nSEC located west of 32° W. This is consistent with the increase of the nSEC intensity observed along section 4, compared to the nSEC intensity captured along section 6, between February and May (Fig. 5b).

During the second half of the year, Fig. 8 shows a wider NECC which extends north of 10°N. During boreal fall, the NECC flow is formed by a nNECC branch separated from the initial sNECC branch during between 38°-48° W, that meet east of 38° W. This is consistent with Fig. 4 S5-S6. During boreal summer, the nNECC branch seems to be supplied by the northern part of the NBC retroflection. This connection seems to fade during boreal fall.

In the equatorial region (2° S-2° N), Fig. 8 also shows the ESC with lower intensity. It appears to be extended east of 32° W and is stronger during boreal spring and fall. This feature can be related to the near-surface eastward flow mentioned previously by Hisard and Hénin (1987) and Bourlès et al. (1999b) on top of the EUC in the WTA. Hisard and Hénin (1987) explained the poor description of this current in the literature by the difficulty of ADCP measurements to fully capture the upper layer currents in this area. They showed that this near-surface current, independent from the EUC, can reach amplitudes larger than 0.5 m s^{-1} between 23° W and 28° W. Comparing their current values to the ESC intensity in our study, we conclude that the weaker values found here (mostly towards 32°W: Fig. 5b) might be explained by the importance of the ageostrophic components of the currents which are not considered here.

For the first time, the seasonal cycle of the ESC has been analyzed in Sect. 4.4 of this study (Fig. 4S4, S5, S6 and Fig. 5b). It is similar to the seasonal cycle of the EUC (semi-annual cycle

632 with two maxima: Brandt et al., 2016; Hormann et al., 2007), which might be due to the fact
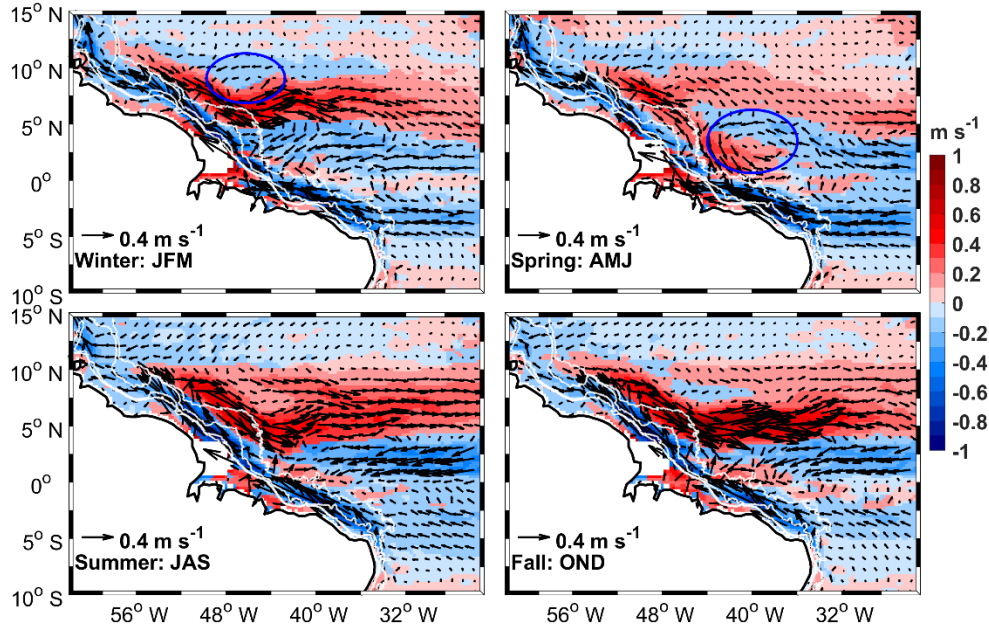633 that most part of the flow is fed by the rNBC.

634

Figure 8. Seasonal maps of the geostrophic currents in the western tropical Atlantic over the 1993-2017 period for boreal winter (top left panel: JFM for January-February-March), boreal spring (top right panel: AMJ for April-May-June), boreal summer (bottom left panel: JAS for July-August-September:) and boreal fall (bottom right panel: OND for October-November-December:). The velocity vectors are superimposed on the speed multiplied by the sign of their zonal components (m s^{-1}). The two cyclonic circulations observed during boreal winter and spring are indicated by blue ellipses. The white lines near to the continent are from west to east, the 300 m, 1000 m, 3000 m and 4000 m isobaths.

643

644 Finally, from all the analyses of the currents carried out above, we propose a new scheme of
645 the seasonal variations of the western boundary tropical Atlantic circulation (Fig. 9). The new
646 current branches found in this study are indicated in green and the currents coming from the
647 north/south are in blue/orange. The width of the current arrows is proportional to the intensity
648 of the current and the dotted arrows represent the currents with the minimum amplitudes. More
649 arrows are put for some currents to show the spatial variability. C1 and C2 are for respectively,
650 the cyclonic circulations highlighted between 44°-50° W and 35°-45° W.
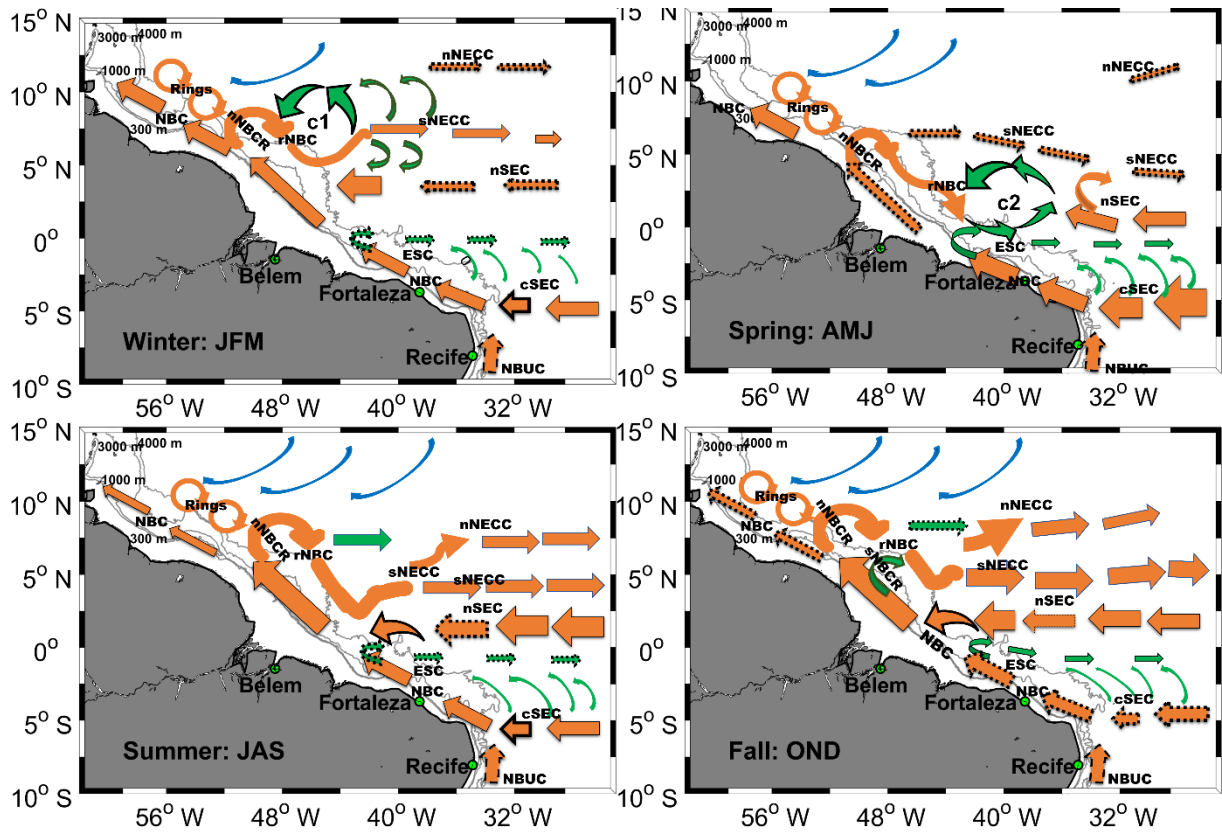
651

652

653

Figure 9. Schematic view of the seasonal maps of the tropical western boundary surface circulation together with the subsurface NBUC signature at the surface. C1 and C2 represent the cyclonic circulations highlighted in this study. The size of the arrows is wider when the intensity of the current is maximum (normal arrows), and decreases with season to reach its minimum (dotted thin line). The NBUC is represented because of its contribution to the NBC transport and is shown by dashed arrows. The current branches which are already known are in orange/blue (orange/blue for the current fed by southern/northern hemisphere water). The green arrows characterize the new branches observed. NBC is the North Brazil Current; nNBCR and sNBCR are the northern and the southern flows of the North Brazil Current retroflection, respectively; rNBC is the retroflected branch of North Brazil current; nNECC and sNECC are the northern and the southern branches of the North Equatorial Countercurrent (NECC), respectively; cSEC and nSEC are the central and the northern branches of the South Equatorial Current (SEC), respectively; and ESC is the Equatorial Surface Current.

Concerning the interannual variability, Hormann et al. (2012), based on the analyses of 17 year of altimetry and drifter' data, found interesting scenarios about the NECC spatial and temporal variability. However, they did not separate the sNECC from the nNECC. In their study, the authors have associated the strengthening of the NECC in the whole basin to the negative phase of the AZM, and its northward shift to the positive phase of the AMM. Our results show different behaviors of the NECC system as a function of the branch and core location. We also showed possible relationships between the southern NECC branch intensity and location with

674   the AMM phases at 42° W, and conversely a possible relationship between the southern NECC

675   branch intensity and location with the AZM phases at 32° W. These results open the way to

676   deeper investigations in future studies.

677   ## 7   Summary and Perspectives

678   Twenty-five years (1993-2017) of gridded altimetry data from CMEMS were used to improve

679   the description of the seasonal and interannual variations of the western boundary circulation

680   of the tropical Atlantic. To do so, a new approach based on the calculation of the current

681   intensity was adopted, using six defined horizontal sections. These sections have been designed

682   to intersect the path of the principal upper ocean flows over the west tropical Atlantic.

683   Copernicus Climate Service ERA5 wind estimates and the NOAA OI SST v2 product were also

684   used to investigate the possible link between the variability of the regional circulation and the

685   large-scale remote wind forcing on the one hand, and the tropical Atlantic climate modes on

686   the other hand.

687   Our results highlight a complex regional circulation, with significant seasonal and year-to-year

688   variations of the current's intensity and location. South of the equator, we observe a

689   stronger/weaker central branch of the South Equatorial Atlantic (cSEC) and of the North Brazil

690   Current (NBC) during boreal spring/fall. North of the equator, the NBC component flowing

691   along the Guyana coast exhibits a similar annual cycle. However, between both, the NBC part

692   located before the retroflection is out of phase (i.e. stronger during summer-fall), when fed by

693   the northern branch of the South Equatorial Current (nSEC). Its larger amplitudes appear during

694   boreal fall, 3-4 months after the maximum of the remote wind stress curl (WSC) strength (in

695   August). The North Equatorial Countercurrent (NECC) is connected with the retroflected

696   branch of the NBC, and both show similar annual cycle. A secondary North Brazil Current

697   Retroflection (NBCR) was observed for the first time during boreal fall in this study: it is

698   located between 4°-6° N. The two-core/branch structure of the NECC during the second half of

699   the year was also confirmed and analyzed separately. Between 0°-5° N and 35°-45° W, a surface

700   cyclonic circulation develops during boreal spring. It is found to initiate the growth of the

701   NECC at 42° W in June. However, at 32° W, the NECC doesn't show any connection with this

702   cyclonic circulation, but starts its seasonal cycle earlier in April when the ITCZ migrates

703   northward and the remote WSC strengthens. In the equatorial region, between 2° S-2° N, the

704   geostrophic currents show the presence of an eastward Equatorial Surface Current (ESC) which

705 has a seasonal cycle similar to the Equatorial Undercurrent (EUC). However, the ageostrophic
706 velocities need to be considered here to fully understand the surface circulation.

707 The interannual variability is much weaker than the seasonal one. It is more important in the
708 eastern part of our study area and there is no obvious regional pattern of low frequency
709 variations. The analysis of the changes in characteristics of the different current branches
710 (intensity and core location), with respect to the tropical Atlantic climate modes, shows
711 different possible scenarios associated with one or both modes. It opens the way for further
712 investigations concerning the link between the Atlantic climate modes (ACM) and the current
713 transports, not possible with altimetry alone.

714 As a conclusion, this study demonstrates the ability of altimetry to characterize the seasonal
715 and interannual variability of the surface circulation in the study area. It confirms previous
716 findings but also significantly complements the knowledge of the different currents at regional
717 scale. Combined use of regional modelling, altimetry and in-situ observations will allow us to
718 go further in the understanding of the spatial and temporal structure of the regional circulation.
719 The intraseasonal variability, significant in the near-shore region of the study area (Fig. 2d) is
720 not studied here. It will be the subject of a future work, based on a coastal altimetry product
721 that will allow a significantly better resolution and accuracy along the continental shelf,
722 compared to a gridded product.

Authors contribution

724 Djoirka M. Dimoune performed the data analyses as part of his PhD thesis. Fabrice Hernandez
725 provided complementary analyses. Florence Birol, Fabrice Hernandez, Fabien Leger and
726 Moacyr Araujo supervised this research.

Competing interests

728 The authors declare that they have no conflict of interest.

References

Aguedjou, H. M. A., Dadou, I., Chaigneau, A., Morel, Y., and Alory, G.: Eddies in the Tropical Atlantic Ocean and their seasonal variability, Geophys. Res. Lett., *46*(21), 12156-12164, https://doi.org/10.1029/2019GL083925, 2019.

Araujo, M., Noriega, C., Hounsou-Gbo, G. A., Veleda, D., Araujo, J., Bruto, L., Feitosa, F., Flores-Montes, M., Lefèvre, N., Melo, P., Ostuska, A., Travassos, K., Schwamborn, R., Neumann-Leitão, S.: A synoptic assessment of the amazon river-ocean continuum during boreal autumn: From physics to plankton communities and carbon flux, Front. Microbiol., 8, 1358, https://doi.org/10.3389/fmicb.2017.01358, 2017.

Arbic, B. K., Scott, R. B., Chelton, D. B., Richman, J. G., and Shriver, J. F.: Effects of stencil width on surface ocean geostrophic velocity and vorticity estimation from gridded satellite altimeter data, J. Geophys. Res.-Oceans, 117(C3), https://doi.org/10.1029/2011jc007367, 2012.

Aroucha, L. C., Veleda, D., Lopes, F. S., Tyaquiçã, P., Lefèvre, N., and Araujo, M.: Intra-and Inter-Annual Variability of North Brazil Current Rings Using Angular Momentum Eddy Detection and Tracking Algorithm: Observations From 1993 to 2016, J. Geophys. Res.-Oceans, 125(12), e2019JC015921, https://doi.org/10.1029/2019jc015921, 2020.

Burmeister K., Lübbecke, J. F.,Brandt, P., and Duteil, O.: Interannual variability of the Atlantic North Equatorial Undercurrent and its impact on oxygen, J. Geophys. Res.-Oceans, 124, 2348–2373, https://doi.org/10.1029/2018JC014760, 2019.

763   Bourles, B., Molinari, R. L., Johns, E., Wilson, W. D., and Leaman, K. D.: Upper layer

764   currents in the western tropical North Atlantic (1989–1991), J. Geophys. Res.-Oceans,

765   104(C1), 1361-1375, https://doi.org/10.1029/1998jc9000250, 1999.

766   Bourlès, B., Gouriou, Y., and Chuchla, R.: On the circulation in the upper layer of the western

767   equatorial Atlantic, J. Geophys. Res.-Oceans, 104(C9), 21151-21170,

768   https://doi.org/10.1029/1999jc900058, 1999.

769   Brandt, P., Schott, F. A., Provost, C., Kartavtseff, A., Hormann, V., Bourlès, B., and Fischer,

770   J.: Circulation in the central equatorial Atlantic: Mean and intraseasonal to seasonal

771   variability, Geophys. Res. Lett., 33(7), https://doi.org/10.1029/2005gl025498, 2006.

772   Brandt, P., Claus, M., Greatbatch, R. J., Kopte, R., Toole, J. M., Johns, W. E., and Böning, C.

773   W.: Annual and semiannual cycle of equatorial Atlantic circulation associated with basin-

774   mode resonance, J. Phys. Oceanogr., 46(10), 3011-3029, https://doi.org/10.1175/jpo-d-15-

775   0248.1, 2016.

776   Cabos, W., de la Vara, A., and Koseki, S.: Tropical Atlantic variability: observations and

777   modelling, Atmosphere, 10(9), 502, https://doi.org/10.3390/atmos10090502, 2019.

778   Cochrane, J. D., Kelly Jr, F. J., and Olling, C. R.: Subthermocline countercurrents in the

779   western equatorial Atlantic Ocean, J. Phys. Oceanogr., *9*(4), 724-738,

780   https://doi.org/10.1175/1520-0485(1979)009<0724:scitwe>2.0.co;2, 1979.

781   Didden, N., and Schott, F.: Seasonal variations in the western tropical Atlantic: Surface

782   circulation from Geosat altimetry and WOCE model results, J. Geophys. Res.-Oceans,

783   97(C3), 3529-3541, https://doi.org/10.1029/91jc02860, 1992.

784   Dossa, A. N., Silva, A. C., Chaigneau, A., Eldin, G., Araujo, M., and Bertrand, A.: Near-

785   surface western boundary circulation off Northeast Brazil, Prog. Oceanogr., 190, 102475,

786   https://doi.org/10.1016/j.pocean.2020.102475, 2021.

787   Ffield, A.: North Brazil current rings viewed by TRMM Microwave Imager SST and the

788   influence of the Amazon Plume, Deep-Sea Res. Pt. I, 52(1), 137-160,

789   https://doi.org/10.1016/j.dsr.2004.05.013, 2005.

790   Fonseca, C. A., Goni, G. J., Johns, W. E., and Campos, E. J.: Investigation of the north Brazil

791   current retroflection and north equatorial countercurrent variability, Geophys. Res. Lett.,

792   31(21), https://doi.org/10.1029/2004gl020054, 2004.

793 Fratantoni, D. M., Johns, W. E., Townsend, T. L., and Hurlburt, H. E.: Low-latitude

794 circulation and mass transport pathways in a model of the tropical Atlantic Ocean, J. Phys.

795 Oceanogr., 30(8), 1944-1966,

796 https://doi.org/10.1175/15200485(2000)030<1944:LLCAMT>2.0.CO;2, 2000.

797 Garzoli, S. L., and Katz, E. J.: The forced annual reversal of the Atlantic North Equatorial

798 Countercurrent, J. Phys. Oceanogr., 13(11), 2082-2090, https://doi.org/10.1175/1520-

799 0485(1983)013<2082:tfarot>2.0.co;2, 1983.

800 Garzoli, S. L.: The Atlantic North Equatorial Countercurrent: Models and observations, J.

801 Geophys. Res.-Oceans, 97 (C11), 17931-17946, https://doi.org/10.1029/92jc01363, 1992.

802 Garzoli, S. L., Ffield, A., and Yao, Q.: North Brazil Current rings and the variability in the

803 latitude of retroflection, Elsevier Oceanogr. Ser., 68, 357-373, https://doi.org/10.1016/s0422-

804 9894(03)80154-x, 2003.

805 Garzoli, S. L., Ffield, A., Johns, W. E., and Yao, Q.: North Brazil Current retroflection and

806 transports, J. Geophys. Res.-Oceans, 109(C1), https://doi.org/10.1029/2003jc001775, 2004.

807 Garzoli, S. L., and Matano, R.: The South Atlantic and the Atlantic meridional overturning

808 circulation, Deep-Sea Res. II, 58(17-18), 1837-1847,

809 https://doi.org/10.1016/j.dsr2.2010.10.063, 2011.

810 Gill, A. E., and Adrian, E.: Atmosphere-ocean dynamics, Vol. 30, Academic press,

811 https://doi.org/10.1016/s0074-6142(08)60025-x, 1982.

812 Góes, M., and Wainer, I.: Equatorial currents transport changes for extreme warm and cold

813 events in the Atlantic Ocean, Geophys. Res. Lett., 30(5),

814 https://doi.org/10.1029/2002gl015707, 2003.

815 Goes, M., Molinari, R., da Silveira, I., and Wainer, I.: Retroflections of the north brazil

816 current during february 2002, Deep-Sea Res. Pt. I, *52*(4), 647-667,

817 https://doi.org/10.1016/j.dsr.2004.10.010, 2005.

818 Goni, G. J., and Johns, W. E.: Synoptic study of warm rings in the North Brazil Current

819 retroflection region using satellite altimetry, Elsevier Oceanogr. Ser., 68, 335-356,

820 https://doi.org/10.1016/s0422-9894(03)80153-8, 2003.

Hazeleger, W., and De Vries, P.: Fate of the Equatorial Undercurrent in the Atlantic, Elsevier Oceanogr. Ser., 68, 175-191, https://doi.org/10.1016/s0422-9894(03)80146-0, 2003.

Hazeleger, W., de Vries, P., and Friocourt, Y.: Sources of the Equatorial Undercurrent in the Atlantic in a high-resolution ocean model, J. Phys. Oceanogr., 33(4), 677-693, https://doi.org/10.1175/1520-0485(2003)33<677:soteui>2.0.co;2, 2003.

Hisard, P., and Hénin, C.: Response of the equatorial Atlantic Ocean to the 1983–1984 wind from the Programme Français Océan et Climat dans l'Atlantique Equatorial cruise data set, J. Geophys. Res.-Oceans, 92(C4), 3759-3768, https://doi.org/10.1029/jc092ic04p03759, 1987.

Hormann, V., and Brandt, P.: Atlantic Equatorial Undercurrent and associated cold tongue variability, J. Geophys. Res.-Oceans, 112(C6), https://doi.org/10.1029/2006jc003931, 2007.

Hormann, V., Lumpkin, R., and Foltz, G. R.: Interannual North Equatorial Countercurrent variability and its relation to tropical Atlantic climate modes, J. Geophys. Res.-Oceans, 117(C4), https://doi.org/10.1029/2011jc007697, 2012.

Jochum, M., and Malanotte-Rizzoli, P.: On the generation of North Brazil Current rings, J. Mar. Res., 61(2), 147-173, https://doi.org/10.1357/002224003322005050, 2003.

Johns, W. E., Lee, T. N., Schott, F. A., Zantopp, R. J., and Evans, R. H.: The North Brazil Current retroflection: Seasonal structure and eddy variability, J. Geophys. Res.-Oceans, 95(C12), 22103-22120, https://doi.org/10.1029/jc095ic12p22103, 1990.

Johns, W. E., Lee, T. N., Beardsley, R. C., Candela, J., Limeburner, R., and Castro, B.: Annual cycle and variability of the North Brazil Current, J. Phys. Oceanogr., *28*(1), 103-128, https://doi.org/10.1175/1520-0485(1998)028<0103:acavot>2.0.co;2, 1998.

Lagerloef, G. S., Mitchum, G. T., Lukas, R. B., and Niiler, P. P.: Tropical Pacific near-surface currents estimated from altimeter, wind, and drifter data, J. Geophys. Res.-Oceans, 104(C10), 23313-23326, https://doi.org/10.1029/1999jc900197, 1999.

Large, W. G., and Pond, S.: Open ocean momentum flux measurements in moderate to strong winds, J. Phys. Oceanogr., 11(3), 324-336, https://doi.org/10.1175/1520-0485(1981)011<0324:oomfmi>2.0.co;2, 1981.

Luko, C. D., da Silveira, I. C. A., Simoes-Sousa, I. T., Araujo, J. M., and Tandon, A.: Revisiting the Atlantic South Equatorial Current, J. Geophys. Res.-Oceans, 126, e2021JC017387, doi: https://doi.org/10.1029/2021JC017387, 2021.

851   NRSC: OSCAT Wind stress and Wind stress curl products, Ocean Sciences Group, Earth and

852   Climate Science Area, Hyderabad, India, 18 pp., 2013.

853   Peterson, R. G., and Stramma, L.: Upper-level circulation in the South Atlantic Ocean, Prog.

854   Oceanogr., 26(1), 1-73, https://doi.org/10.1016/0079-6611(91)90006-8, 1991.

855   Provost, C., Arnault, S., Chouaib, N., Kartavtseff, A., Bunge, L., and Sultan, E.:

856   TOPEX/Poseidon and Jason equatorial sea surface slope anomaly in the Atlantic in 2002:

857   Comparison with wind and current measurements at 23W, Mar. Geod., 27(1-2), 31-45,

858   https://doi.org/10.1080/01490410490465274, 2004.

859   Pujol, M. I., Faugère, Y., Taburet, G., Dupuy, S., Pelloquin, C., Ablain, M., and Picot, N.:

860   DUACS DT2014: the new multi-mission altimeter data set reprocessed over 20 years, Ocean

861   Sci., 12(5), 1067-1090, https://doi.org/10.5194/os-2015-110, 2016.

862   Richardson, P. L., and Walsh, D.: Mapping climatological seasonal variations of surface

863   currents in the tropical Atlantic using ship drifts, J. Geophys. Res.-Oceans, 91(C9), 10537-

864   10550, https://doi.org/10.1029/jc091ic09p10537, 1986.

865   Rodrigues, R. R., Rothstein, L. M., and Wimbush, M.: Seasonal variability of the South

866   Equatorial Current bifurcation in the Atlantic Ocean: A numerical study, J. Phys. Oceanogr.,

867   37(1), 16-30, https://doi.org/10.1175/jpo2983.1, 2007.

868   Schmitz Jr, W. J., and McCartney, M. S.: On the north Atlantic circulation, Rev. Geophys.,

869   31(1), 29-49, https://doi.org/10.1029/92RG02583, 1993.

870   Schott, F. A., Stramma, L., and Fischer, J.: The warm water inflow into the western tropical

871   Atlantic boundary regime, spring 1994, J. Geophys. Res.-Oceans, 100(C12), 24745-24760,

872   https://doi.org/10.1029/95jc02803, 1995.

873   Schott, F. A., Fischer, J., and Stramma, L.: Transports and pathways of the upper-layer

874   circulation in the western tropical Atlantic, J. Phys. Oceanogr., 28(10), 1904-1928,

875   https://doi.org/10.1175/1520-0485(1998)028<1904:tapotu>2.0.co;2, 1998.

876   Schott, F. A., McCreary Jr, J. P., and Johnson, G. C.: Shallow overturning circulations of the

877   tropical-subtropical oceans, Washington DC American Geophysical Union Geophys. Monogr.

878   Ser., 147, 261-304, https://doi.org/10.1029/147gm15, 2004.

879   Servain, J.: Simple climatic indices for the tropical Atlantic Ocean and some applications, J.

880   Geophys. Res.-Oceans, 96 (C8), 15137-15146, https://doi.org/10.1029/91jc01046, 1991.

881   Silva, M., Araujo, M., Servain, J., Penven, P., and Lentini, C. A.: High-resolution regional

882   ocean dynamics simulation in the southwestern tropical Atlantic. Ocean Model., 30(4), 256-

883   269, https://doi.org/10.1016/j.ocemod.2009.07.002, 2009.

884   Stramma, L., and Schott, F.: The mean flow field of the tropical Atlantic Ocean, Deep-Sea

885   Res. Pt. II, 46(1-2), 279-303, https://doi.org/10.1016/s0967-0645(98)00109-x, 1999.

886   Stramma, L., and England, M.: On the water masses and mean circulation of the South

887   Atlantic Ocean, J. Geophys. Res.-Oceans, 104(C9), 20863-20883,

888   https://doi.org/10.1029/1999JC900139, 1999.

889   Sudre, J., Maes, C., and Garçon, V.: On the global estimates of geostrophic and Ekman

890   surface currents, Limnol. Oceanogr.: Fluids Environ., 3(1), 1-20,

891   https://doi.org/10.1215/21573689-2071927, 2013.

892   Trenberth, K. E., Large, W. G., and Olson, J. G.: The mean annual cycle in global ocean wind

893   stress, J. Phys. Oceanogr., 20(11), 1742-1760, https://doi.org/10.1175/1520-

894   0485(1990)020<1742:TMACIG>2.0.CO;2, 1990.

895   Tuchen, F. P., Lübbecke, J. F., Schmidtko, S., Hummels, R., and Böning, C. W. : The Atlantic

896   subtropical cells inferred from observations, J. Geophys. Res.-Oceans, *124*(11), 7591-7605,

897   https://doi.org/10.1029/2019JC015396, 2019.

898   Tuchen, F. P., Lübbecke, J. F., Brandt, P., and Fu, Y.: Observed transport variability of the

899   Atlantic Subtropical Cells and their connection to tropical sea surface temperature variability.

900   J. Geophys. Res.-Oceans, *125*(12), e2020JC016592, https://doi.org/10.1029/2020JC016592,

901   2020.

902   Tuchen, F.P., Brandt, P., Lübbecke, J. F., and Hummels, R.: Transports and Pathways of the

903   Tropical AMOC Return Flow From Argo Data and Shipboard Velocity Measurements. J.

904   Geophys. Res.-Oceans, 127 (2), e2021JC018115, https://doi.org/10.1029/2021JC018115,

905   2022.

906   Urbano, D. F., Jochum, M., and Da Silveira, I. C. A.: Rediscovering the second core of the

907   Atlantic NECC, Ocean model., 12(1-2), 1-15, https://doi.org/10.1016/j.ocemod.2005.04.003,

908   2006.

909 Urbano, D. F., De Almeida, R. A. F., and Nobre, P.: Equatorial Undercurrent and North

910 Equatorial Countercurrent at 38 W: A new perspective from direct velocity data, J. Geophys.

911 Res.-Oceans, 113(C4), https://doi.org/10.1029/2007jc004215, 2008.

912 Verdy, A., and Jochum, M.: A note on the validity of the Sverdrup balance in the Atlantic

913 North Equatorial Countercurrent, Deep-Sea Res. Pt. I, 52(1), 179-188,

914 https://doi.org/10.1016/j.dsr.2004.05.014, 2005.

915 Zebiak, S. E.: Air–Sea Interaction in the Equatorial Atlantic Region, J. Clim., 6 (8), 1567-

916 1586, https://doi.org/10.1175/1520-0442(1993)006<1567:AIITEA>2.0.CO;2, 1993.

917 Zheng, Y., and Giese, B. S.: Ocean heat transport in simple ocean data assimilation: Structure

918 and mechanisms, J. Geophys. Res.-Oceans, 114(C11), https://doi.org/10.1029/2008jc005190,

919 2009.